A novel concept for reducing wave reflection from OWC structures with application of harbor agitation mitigation/coastal protection: theoretical investigations

Yang Zhang[1], Xuanlie Zhao[1*], Jing Geng[1], Longbin Tao[2]

1. College of Shipbuilding Engineering, Harbin Engineering University, Harbin, 150001, China
2. Department of Naval Architecture, Ocean & Marine Engineering, University of Strathclyde, Glasgow G4 0LZ, United Kingdom

*Corresponding author: Xuanlie Zhao (xlzhao@hrbeu.edu.cn)

Abstract: By using wave energy dissipating/capturing capability of the perforated structure and wave absorbers to reduce the wave reflection from the harbor/coast, this paper describes a theoretical study on the hydrodynamic performance of a novel OWC structure, comprising of a harbor/coast-based OWC device provided with a surface-piercing perforated barrier. An analytical model of wave interaction with the novel OWC structure was developed, based on the linear potential theory. The effects of geometric configurations on hydrodynamic coefficients were revealed. The results show that a remarkable reduction of reflection coefficient (up to 80%) from the novel OWC structure was realized, with the second benefit of a satisfactory wave power extraction efficiency. The incident wave energy is absorbed by OWC device in lower frequency region and is dissipated by a perforated wall in higher frequency region, respectively. The dissipation of a perforated wall slightly affects the power extraction by OWC. In addition, the location of a perforated wall is identified as a key parameter influencing the performance of this novel OWC structure. It is worth noting that the presence of a perforated wall cannot avoid the sloshing-mode resonance of the OWC, accompanied by the strong reflection.

Keywords: harbor agitation reduction, coastal protection, wave reflection, perforated wall, oscillating water column, wave force.

This is a peer-reviewed, accepted author manuscript of the following paper: Zhang, Y., Zhao, X., Geng, J., & Tao, L. (2021). A novel concept for reducing wave reflection from OWC structures with application of harbor agitation mitigation/coastal protection: theoretical investigations. Ocean Engineering, 242, [110075]. https://doi.org/10.1016/j.oceaneng.2021.110075

1 Introduction and motivations

In coastal engineering, vertical wall-type structures are frequently used to prevent the harbor or coastline from the wave impact, but greater reflection will occur on the windward side. The wave attenuation is not superior to rubble-mound structures (Altomare and Gironella, 2014), but with an advantage of economic competitiveness (i.e., shallow/deep-water applications and the less occupied area). Wave reflection from harbor structures harms the safety of the maneuvering, berthing, and loading operations inside the harbor. Therefore, reducing the wave reflection at vertical wall structures is an important method. Several low-reflectivity structures have been presented (Huang et al., 2011; Simonetti and Cappietti, 2021).

The perforated wall with wave energy dissipation capacity by the turbulence, friction losses, vortices, and resonance effects, is used to reduce the wave reflection and wave loads acting on the caisson front wall (Liu et al. 2018). Detailly, Jarlan-type breakwater caissons (Huang et al., 2011) with one or more dissipative wave chambers have an exposed perforated wall(s) and a rear wall. Lee and Shin (2014) investigated experimentally the wave reflection of partially perforated wall caissons with double chambers, and the wave attenuation was determined by comparisons between the front wall and middle wall porosity. Liu et al. (2016) presented the influence of the plain and partially perforated walls located in front of the caisson on the wave evolution experimentally. The along-shore direction sidewall was an important factor than the porosity for evaluating the reflection coefficient. Theocharis et al. (2011) introduced a wave-absorbing quay-wall with a partial chamber, with an impermeable back wall. The experimental investigation showed that a reduction of wave height in front of the wall (i.e., 20–30%) was found. López et al. (2018) proposed a novel perforated-wall caisson concept, the LOW Reflection Breakwater, based on a three-chamber, perforated-wall, and inner weirs. Neelamani et al. (2017) assessed experimentally the wave reflection of slotted vertical barriers with an impermeable rear wall. A reduction in wave height (i.e., 20–30%) and minimum reflection coefficients of 0.3 were obtained. Above the kinds of literature, the perforated wall passively reduces the wave reflection, by dissipating the wave energy into turbulent kinetic energy and reflected energy. Additionally, wave absorbers can be regarded as an active method to further reduce the wave reflection, by converting the incident wave energy into electric power.

According to the wave energy conversion principle, wave energy converters (WECs) are divided into the oscillating water column (OWC), oscillating body, and overtopping device. Most of the devices are in the stage of laboratory tests and some are in the stage of the trial/field test (Zhao et al., 2019). The OWC WEC is regarded as one of the most promising renewable energy devices, due to its mechanical and structural simplicity. It can be embedded in a harbor, shorelines, or coastal structures (i.e., breakwater) (Melikoglu, 2018), which also increases the accessibility of the wave energy technology. The full-scale prototype OWC devices consist of OSPREY, Pico, Sakata, LIMPET, Mutriku, Yongsoo, and REWEC3 (Mustapa et al., 2017).

The performance of OWC devices was widely investigated by optimizing the geometrical configuration (Zhao et al., 2021a and 2021b), with a focus on the efficiency or the effective frequency bandwidth (Teixeira and Didier, 2021). The concept of a multiple-chamber OWC device was developed recently to broaden the effective frequency bandwidth (Ning et al., 2018). Rezanejad et al. (2015) found that an efficiency increment and broader frequency bandwidth were achieved due to the multiple wave resonances with a stepped sea bottom. Due to the wave power extraction, the OWC device can be regarded as an anti-reflection device to reduce wave reflection from a vertical wall (i.e., embedded in vertical wall/caisson breakwater/coastline, etc.). He and Huang (2016) found that an OWC device in front of the vertical wall could function as effectively as the slotted-barrier-type wave absorbers to reduce the wave reflection, with a potential to extract wave energy for electricity generation. Simonetti and Cappietti (2021) also investigated the hydraulic performance of an OWC device as an anti-reflection device integrated into a vertical wall harbor structure. The results showed that mitigation of wave reflection (i.e., 15%) of OWC device could be found and efficiently be used to reduce wave agitation in front of vertical wall harbor.

For benefits of wave reflection reduction, however, an OWC device is anticipated to work not only promoting efficiency but also enduring the large wave force impact on harbor structures during storms. The reliability of devices is an important consideration for practical design and construction. Several full prototype nearshore OWC devices (i.e., OSPREY, greenWAVE, Mutriku, and Pico plant) were destroyed from storms during operation or construction (Medina-López et al., 2015; Falcão and Henriques, 2020). Among these, the front wall of the OWC device is in an

essential position. The wave forces acting on caissons embodying a U-OWC and stability were evaluated by Boccotti (2012). John Ashlin et al. (2015) found that the peak horizontal wave force acting on the OWC device is more than 2.5 to 3 times the vertical force. Viviano et al. (2019) presented the wave forces acting on a large-scale OWC device under random waves and regular waves and found that the force formula for vertical walls is not valid for OWC devices. Ning et al. (2020) analyzed the effect of geometrical parameters, wave conditions, and viscosity on wave force acting on an OWC device. Pawitan et al. (2019) found that the vertical force on a caisson OWC-breakwater significantly affected the overturning and sliding. Wang et al. (2020) investigated the wave loads acting on a dual-chamber OWC device. It was found that the wave force seaside curtain wall is dominant, and the largest wave-induced bending moment occurred at the joint of the device and seabed. Therefore, reducing the wave loads determines the safety of a land-based OWC device remarkably, with the function of reducing reflection from the harbor.

Considering that the wave energy dissipation/capturing capability of the perforated wall and an OWC device, an integration between both structures may further mitigate the wave reflection to reduce harbor agitation, with the benefit of improving the device stability. Tsai et al. (2018) proposed an effective structure of breakwater-integrated OWC WEC comprising of a perforated wall in front of a typical OWC chamber. The wave power extraction and a reduction of the wave force were realized. The underlying physical mechanism of reflection reduction was not well revealed for different geometrical configurations, due to whether the OWC captures wave energy or the perforated wall dissipates energy. Motivated by caisson breakwater embedded in a harbor wall as the function of wave power extraction (i.e., Mutriku wave power plant) and the coastal defense (i.e., Jarlan structure), to reduce wave reflections from the harbor structure, the further theoretical analysis was presented in this paper, including a surface-piercing perforated barrier in the front of an OWC device, different to Tsai et al. (2018) (i.e., bottom-mounted). Therefore, the configuration of this novel structure resembles a dual-chamber OWC device, which may trigger multiple wave resonances. Also, a perforated wall nearby the water surface may dissipate some incident wave energy to avoid the larger wave force acting on the front wall of the OWC device. By dissipating most wave energy by both structures, wave reflection from this system may further decrease significantly to reduce harbor agitation. Based on the linear

potential flow theory, an analytical model of wave interaction with a novel OWC structure was developed. The effects of geometrical parameters on hydrodynamic coefficients were revealed. The structural stability and the wave power extraction would be further evaluated.

This paper is organized as follows: In Section 2, a mathematical model and hydrodynamic coefficients are introduced and derived. In Section 3, the analytical solutions are validated. In Section 4, results are presented and discussed. Finally, the corresponding conclusions are summarized in Section 5.

2 Mathematical model

2.1 Model description

The sketch and geometry of this novel OWC structure are illustrated in Fig. 1, as well as the 2D Cartesian coordinate system. Two caissons embedded in the harbor/coastline along with incidence waves can be designed as follow: 1) the windward side caisson with the perforated wall as a dissipative chamber; 2) the lee side caisson with the solid wall as an OWC chamber with power take-off (PTO) to extract wave energy. The single OWC WEC is arranged at the coast. *o*-*xy* is employed, and the center of the origin is located at the cross-point of the still water surface and a medial axis of the air chamber. The OWC front wall thickness of 2ε is set in the water depth h. The perforated wall of draft d_1 is placed at a distance $2b$ from the OWC front wall of draft d_2. The incident wavenumber, wave amplitude, angular frequency, wavelength, and period can be expressed as κ_1, A, ω, L and T, respectively.

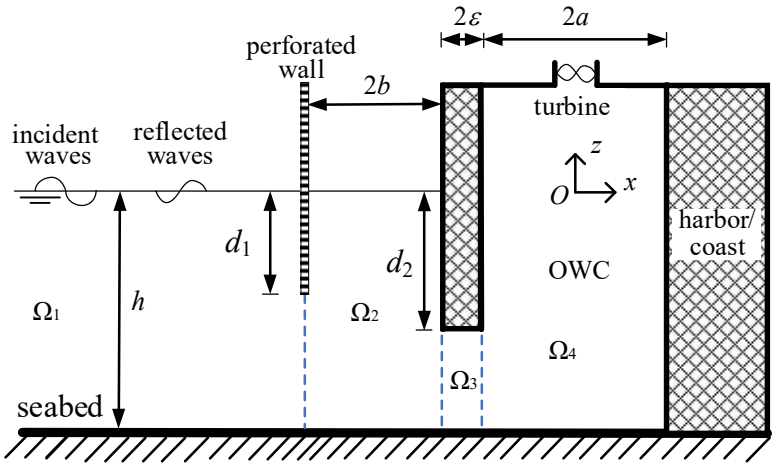

Fig. 1. The sketch of a harbor/coast-based OWC WEC with a perforated wall.

2.2 Governing equation and boundary conditions

For the aspect of the wave interaction with perforated structure, the fluid assumption and boundary condition were derived in Sollitt and Cross (1972) and Yu (1995). Therefore, the whole field can be regarded as the incompressible, potential, and irrotational flow, involving the damping terms at the perforated wall boundary. The thickness of a perforated wall is neglected for the adoption of the irrotational flow model. The wave motion in the whole domain can be depicted by the velocity potential with simple harmonic in the time angular frequency ω:

$$\Phi(x,z,t)=\mathrm{Re}\left[\phi(x,z)\exp(-\mathrm{i}\omega t)\right], \tag{1}$$

where the spatial velocity potential $\phi(x, z)$ satisfies the 2-D Laplace equation:

$$\frac{\partial^2\phi}{\partial x^2}+\frac{\partial^2\phi}{\partial z^2}=0. \tag{2}$$

$\phi(x, z)$ is decomposed as the linear superpositions of scattering and radiation potentials

$$\phi(x,z)=\phi_S(x,z)+p_a\phi_R(x,z), \tag{3}$$

where $\phi_S(x, z)$ denotes the scattering velocity potential, representing the wave field when the system is subjected to incident waves in the absence of air pressure p_a, including the incident and diffracted potential; $\phi_R(x, z)$ denotes the spatial radiation velocity potential due to the unit-amplitude pressure p_a in the absence of incident waves.

As indicated in Fig. 1, the whole fluid domain is divided into four subdomains ($\phi_S^{(n)}$ and $\phi_R^{(n)}$, n = 1, 2, 3 and 4), consisting of Ω_1: $-a < x < a$ and $-h < z < 0$; Ω_2: $-a$-$2\varepsilon < x < -a$ and $-h < z < -d_2$; Ω_3: $-a$-2ε-$2b < x < -a$-2ε and $-h < z < 0$; Ω_4: $-\infty < x < -a$-2ε-$2b$ and $-h < z < 0$. The corresponding boundary conditions of ϕ_ℓ (ℓ = S and R) can be written as

$$\frac{\partial\phi_\ell}{\partial z}=\frac{\omega^2}{g}\phi_\ell \text{ at } z=0, x\le -a, \tag{4}$$

$$\frac{\partial\phi_R}{\partial z}=\frac{\omega^2}{g}\phi_R+\frac{\mathrm{i}\omega}{\rho g} \text{ and } \frac{\partial\phi_S}{\partial z}=\frac{\omega^2}{g}\phi_S \text{ at } z=0, -a\le x\le a, \tag{5}$$

$$\frac{\partial\phi_\ell}{\partial x}=0 \text{ at } x=a, -h\le z\le 0, \tag{6}$$

$$\frac{\partial\phi_\ell}{\partial x}=0 \text{ at } x=-a \text{ and } -a-2\varepsilon, -d_2\le z\le 0, \tag{7}$$

$$\frac{\partial\phi_\ell}{\partial z}=0 \text{ at } z=-h, x\le a, \tag{8}$$

$$\frac{\partial \phi_\ell}{\partial z} = 0 \text{ at } z = -d_2, -a - 2\varepsilon \le x \le -a\,. \tag{9}$$

Based on the mathematical model of wave interaction with porous medium (Sollitt and Cross, 1972) and the boundary condition of the porous thin plate (Yu, 1995), the matching boundary condition of the perforated thin wall in the present model can be illustrated as

$$\frac{\partial \phi_\ell^{(1)}}{\partial x} = \frac{\partial \phi_\ell^{(2)}}{\partial x} = \mathrm{i}\kappa_1 G\left(\phi_\ell^{(1)} - \phi_\ell^{(2)}\right) \text{ at } x = -a - 2b - 2\varepsilon, -d_1 \le z \le 0, \tag{10}$$

where $G = \dfrac{\gamma}{\kappa_1 \delta}\left\{ f - \mathrm{i}\left[1 + \dfrac{C_m(1-\gamma)}{\gamma} \right] \right\}$, δ is the physical thickness of the porous wall (the thickness is negligible geometrically, due to that the thickness of the perforated wall is much smaller in length scale for the wave motion within the porous medium in both directions) and γ, f and C_m are the porosity, the linearized resistance coefficients and the added-mass coefficient of the porous medium, respectively (Yu, 1995). The porosity coefficients G can be expressed as $G_r + \mathrm{i}G_\mathrm{i}$, where represents the drag term and the inertia term, which results in the wave energy loss and the phase change, respectively (Liu and Li, 2011; Lyu et al., 2020; Ning et al., 2017). Additionally, it is required that the $\phi_S^{(n)}$ and $\phi_R^{(n)}$ (n = 1, 2, 3 and 4) are outgoing for $x \to -\infty$.

2.3 Expressions of scattering and radiation velocity potential

By using the method of separation of variables and matching eigenfunction expansion, the $\phi_\ell^{(n)}$(n = 1, 2, 3, 4 and ℓ = S and R) for each fluid region can be expressed as

$$\phi_\ell^{(1)} = -\frac{\mathrm{i}gA}{\omega}\left\{ \mathrm{e}^{-k_1(x+2b+2\varepsilon+a)}\delta_{\ell,S} Z_1(z) + \sum_{n=1}^{+\infty} R_n^\ell \mathrm{e}^{k_n(x+2b+2\varepsilon+a)} Z_n(z) \right\}, \tag{11}$$

$$\phi_\ell^{(2)} = -\frac{\mathrm{i}gA}{\omega}\left\{ \sum_{n=1}^{+\infty}\left(A_n^\ell \mathrm{e}^{-k_n(x+a+2b+2\varepsilon)} + B_n^\ell \mathrm{e}^{k_n(x+a+2\varepsilon)} \right) Z_n(z) \right\}, \tag{12}$$

$$\phi_\ell^{(3)} = -\frac{\mathrm{i}gA}{\omega}\left\{ \left(C_1^\ell x + D_1^\ell \right) + \sum_{n=2}^{+\infty}\left(C_n^\ell \mathrm{e}^{-\lambda_n(x+a+2\varepsilon)} + D_n^\ell \mathrm{e}^{\lambda_n(x+a)} \right) \varphi_n(z) \right\}, \tag{13}$$

$$\phi_\ell^{(4)} = -\frac{\mathrm{i}gA}{\omega}\left\{ \sum_{n=1}^{+\infty} T_n^\ell \frac{\cosh\left[k_n(x-a)\right]}{\cosh\left[2k_n a\right]} Z_n(z) \right\} - \frac{\mathrm{i}\delta_{\ell,R}}{\rho\omega}\,. \tag{14}$$

The $\delta_{\ell,\chi}$ is the Kronecker delta

$$\delta_{\ell,\chi}=\begin{cases}1, \ell=\chi\\ 0, \ell\neq\chi\end{cases}. \tag{15}$$

The $Z_n(z)$ and $\varphi_n(z)$ represent the z-direction eigenfunctions, which can be expressed as

$$Z_n(z)=\frac{\cos\left[k_n(z+h)\right]}{\cos\left[k_n h\right]} \tag{16}$$

and

$$\varphi_n(z)=\cos\left[\lambda_n(z+h)\right], \tag{17}$$

respectively. The k_n are the roots of dispersion relation in k as given by ω^2=-g$k$tan(kh), where the dispersion relation has one imaginary root k_1=-iκ_1 and an infinite number of positive real roots k_n, n = 2, 3, ⋯, with λ_n=(n-1)π/(h-d_2), n = 1, 2, ⋯. The unknown scattering and radiation coefficients R_n^ℓ, A_n^ℓ, B_n^ℓ, C_n^ℓ, D_n^ℓ and T_n^ℓ will be determined.

Mathematically, there exists a strong singularity at the sharp edge of a perforated wall, which may lead to the slow convergence of these solutions. The multi-term Galerkin method proposed by Evans and Porter (1995b) was adopted to handle the velocity singularity. As for a perforated wall, the jump of velocity potentials can be shown as

$$\phi_\ell^{(1)}-\phi_\ell^{(2)}=\begin{cases}0, x=-a-2\varepsilon-2b, -h<z<-d_1,\\ \sum_{s=0}^{+\infty}E_s^\ell p_s(z), x=-a-2\varepsilon-2b, -d_1<z<0,\end{cases} \tag{18}$$

where E_s^ℓ are unknown coefficients corresponding to wave scattering and radiation problem, and $p_s(z)$ is given by

$$\hat{p}_s(z)=p_s(z)-\frac{\omega^2}{g}\int_{-d_1}^{z}p_s(z)\mathrm{d}z \tag{19}$$

with

$$\hat{p}_s(z)=\frac{2(-1)^s\sqrt{d_1^2-z^2}}{\pi(2s+1)d_1 h}U_{2s}\left(-\frac{z}{d_1}\right), -d_1<z<0. \tag{20}$$

The function $U_n(x)$ denotes the nth order Chebychev polynomial of the second kind, which can be expressed by

$$U_n(x)=\frac{\sin\left((n+1)\arccos x\right)}{\sin\left(\arccos x\right)}. \tag{21}$$

The orthogonal relation between the z-component of $p_s(z)$ and the vertical eigenfunction of $Z_n(z)$ is satisfied by

$$\beta_{sn}=\begin{cases}\int_{-d_1}^{0} p_s(z)Z_1(z)dz=\dfrac{(-1)^s I_{2s+1}(\kappa_1 d_1)}{\kappa_1 h}, u=1,\\ \int_{-d_1}^{0} p_s(z)Z_u(z)dz=\dfrac{J_{2s+1}(k_u d_1)}{k_u h}, u=2,3,\ldots\end{cases}, \tag{22}$$

where J_n and I_n denote the Bessel function and modified Bessel function of order n, respectively.

2.4 Solution procedure

The scattering and radiation velocity potential must satisfy conditions for both the pressure and velocity at the interfaces between adjacent subdomains.

$$\frac{\partial \phi_\ell^{(1)}}{\partial x}=\frac{\partial \phi_\ell^{(2)}}{\partial x} \text{ at } x=-2b-2\varepsilon-a, -h\le z\le 0, \tag{23}$$

$$\phi_\ell^{(1)}-\phi_\ell^{(2)}=\begin{cases}0 & \text{at } x=-a-2\varepsilon-2b, -h\le z\le -d_1,\\ \sum_{s=0}^{+\infty} E_s^\ell p_s(z) & \text{at } x=-a-2\varepsilon-2b, -d_1\le z\le 0,\end{cases} \tag{24}$$

$$\partial\phi_\ell^{(2)}/\partial x=\mathrm{i}\kappa_1 G\left(\phi_\ell^{(1)}-\phi_\ell^{(2)}\right) \text{ at } x=-2b-2\varepsilon-a, -d_1\le z\le 0, \tag{25}$$

$$\phi_\ell^{(2)}=\phi_\ell^{(3)} \text{ at } x=-a-2\varepsilon, -h\le z\le -d_2, \tag{26}$$

$$\frac{\partial \phi_\ell^{(2)}}{\partial x}=\begin{cases}\dfrac{\partial \phi_\ell^{(3)}}{\partial x} & \text{at } x=-a-2\varepsilon, -h\le z\le -d_2,\\ 0 & \text{at } x=-a-2\varepsilon, -d_2\le z\le 0,\end{cases} \tag{27}$$

$$\phi_\ell^{(3)}=\phi_\ell^{(4)} \text{ at } x=-a, -h\le d\le -d_2, \tag{28}$$

$$\frac{\partial \phi_\ell^{(4)}}{\partial x}=\begin{cases}\dfrac{\partial \phi_\ell^{(3)}}{\partial x} & \text{at } x=-a, -h\le d\le -d_2,\\ 0 & \text{at } x=-a, -d_2\le z\le 0,\end{cases} \tag{29}$$

Substituting the expressions of velocity potential in Eq.(11) and (12) into Eq. (23), both sides of Eq. (23) are multiplied by $Z_u(z)$, integrating concerning z from -h to 0. The relation can be derived as

$$R_n^\ell=\begin{cases}\delta_{\ell,\mathrm{D}}-A_1^\ell+B_1^\ell \mathrm{e}^{-2k_1 b}, n=1\\ -A_n^\ell+B_n^\ell \mathrm{e}^{-2k_n b}, n=2,3,\ldots\end{cases}. \tag{30}$$

Then, Eq.(11), (12) and (30) are substituted into Eq. (24) and (25). Multiplying both sides

of Eq. (24) by $Z_u(z)$ and integrating concerning z from -h to 0, Eq. (25) by $p_q(z)$ and integrating concerning z from -d_1 to 0. Substituting Eq. (12) ~ (14) into Eq. (26) ~ (29), both sides of Eq. (26) and (28) are multiplied by $\varphi_u(z)$ and integrating concerning z from -h and -d_2, Eq. (27) and (29) are multiplied by $Z_u(z)$ and integrating concerning z from -h and 0. The unknown coefficients (n and u) in z-direction eigenfunctions are truncated to N, unknown coefficients (s and q) in auxiliary functions to S. Considering unknown coefficients R_n^{ℓ} expressed by A_n^{ℓ} and B_n^{ℓ}, inherently, for the wave scattering or radiation problem, the number of unknown coefficients of the velocity potentials (i.e., A_n^{ℓ}, B_n^{ℓ}, C_n^{ℓ}, D_n^{ℓ} and T_n^{ℓ} in Eq. (12) ~ (14)) and auxiliary functions (i.e., E_s^{ℓ} in Eq. (18)) is $5N+S+1$ for $\ell = S$ or R. By implementing the above matching conditions (see Eq. (24) ~ (29)), the set of linear equations with a size of $5N+S+1$ can be obtained, whose solutions denote the unknowns of the scattering or radiation potential. Hence, scattering and radiation velocity potentials (i.e., Eq. (11) ~ (14)) can be determined.

2.5 Hydrodynamic coefficients

1) Hydrodynamic efficiency

The excitation volume flux Q_e can be obtained by the integration of the vertical velocity of the water surface inside the OWC air chamber, determined by the incident and diffraction velocity potential.

$$Q_e = \int_{-a}^{a} \frac{\partial \phi_S^{(4)}}{\partial z}\Big|_{z=0} \mathrm{d}x = -\mathrm{i}A\omega \sum_{n=1}^{+\infty} T_n^S \frac{\tanh\left[2k_n a\right]}{k_n} \tag{31}$$

Correspondingly, the radiation volume flux Q_R can be obtained by radiation velocity potential.

$$Q_R = \int_{-a}^{a} \frac{\partial \phi_R^{(4)}}{\partial z}\Big|_{z=0} \mathrm{d}x = -(c - \mathrm{i}\mu) \tag{32}$$

where c and μ denote the radiation conductance and radiation susceptance (i.e., c=-Re[Q_R] and μ=Im[Q_R]). The relationship between the complex amplitude of the total volume flux and the air pressure can be written as

$$p = \frac{Q_e}{-\mathrm{i}(\mu_{pto} + \mu) + (c_{pto} + c)}, \tag{33}$$

where c_{pto} denotes the damping of the PTO system of OWC, depending on the rotational spend of turbines, their specification and design, and the static air density. μ_{pto} can be expressed as

$$\mu_{pto}=\frac{\omega V}{\upsilon^2\rho_0}, \tag{34}$$

where V is the air chamber volume of the OWC V=0.2ha, υ denotes the sound velocity in air 340 m/s and ρ_0 is the static air density 1 kg/m^3. The time-averaged wave power extraction over one wave period can be expressed as

$$P=\frac{1}{2}\frac{c_{pto}\left|Q_e\right|^2}{(c_{pto}+c)^2+(\mu+\mu_{pto})^2}. \tag{35}$$

The optimal PTO damping (Falnes and Kurniawan, 2020) can be yielded as

$$c_{opt,pto}=\sqrt{c^2+(\mu+\mu_{pto})^2}\ . \tag{36}$$

Therefore, the wave power extraction efficiency for the optimal PTO damping is

$$P=\frac{1}{4}\frac{\left|Q_e\right|^2}{c+\sqrt{c^2+(\mu+\mu_{pto})^2}} \tag{37}$$

and the hydrodynamic efficiency η can be expressed as

$$\eta=\frac{2P}{\rho g A^2 C_g}, \tag{38}$$

where C_g is the group velocity of the incident wave

$$C_g=\frac{\omega}{2\kappa_1}\left[1+\frac{2\kappa_1 h}{\sinh\left(2\kappa_1 h\right)}\right]. \tag{39}$$

The free water surface of the fluid domain can be expressed as

$$\zeta=\left|\frac{\mathrm{i}\omega}{g}\left(\phi_S+p\phi_R\right)\right|_{z=0}\Bigg| \tag{40}$$

2) Reflection and dissipation coefficients

Considering the reflected waves and radiated waves, reflection coefficients can be expressed as

$$K_r=\left|R_1^S+pR_1^R\right|. \tag{41}$$

Based on the energy conservation law, the dissipation coefficients can be written as

$$K_d=1-\eta-K_r^2 \tag{42}$$

3) Horizontal wave force acting on the front wall of OWC and bending moment

The wave force acting on the front wall and bending moment is a key factor to evaluate the

survivability of the OWC device (Wang et al., 2020). The horizontal wave force, bending moment and rotation center are illustrated in Fig. 2. The horizontal wave force acting on the front wall of OWC can be divided into two parts: F_{x+} and F_{x-} along with positive and negative x-axis direction, respectively. The horizontal wave force F_{H} can be calculated by

$$F_{\mathrm{H}} = \left| F_{x+} \right|_{x=-a-2\varepsilon} - F_{x-} \left|_{x=-a} \right| . \tag{43}$$

$$F_{x+} - F_{x-} = \mathrm{i}\rho\omega \int_{-d_2}^{0} \left[\left(\phi_S^2 + p\phi_R^2 \right) \right|_{x=-a-2\varepsilon} - \left(\phi_S^4 + p\phi_R^4 \right) \Big|_{x=-a} \Big] \mathrm{d}z \tag{44}$$

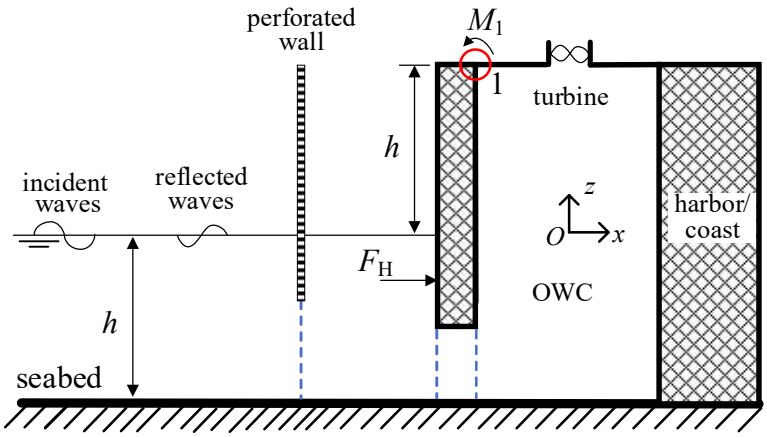

Fig. 2. Schematic of horizontal wave force, bending moment and rotation center.

The moment component M_1 represents the moment about rotation center by horizontal wave force F_{H}. The height of the front wall above the static water surface is assumed h, identical to the water depth. The expressions of M_1 can be written as

$$M_1 = \mathrm{i}\rho\omega \int_{-d_2}^{0} \left[\left(\phi_S^2 + p\phi_R^2 \right) \right|_{x=-a-2\varepsilon} - \left(\phi_S^4 + p\phi_R^4 \right) \Big|_{x=-a} \Big] (h - z) \mathrm{d}z \tag{45}$$

3 Model Validations

3.1 Convergence analysis

Firstly, we analyzed how many terms in infinite sums in potentials and multi-term Galerkin solution must be used to reach the convergence. Geometrical parameters were set for d_1/h = d_2/h = 1/2, b/h = a/h = 1/5, ε/h = 1/10, G = 1 + 1i and the optimal PTO damping. The reflection coefficients K_r at different truncated numbers N and S are calculated. It is found that enough convergence is obtained when N = 80 and S = 5.

3.2 Haskind relationship and energy conservation law

The Haskind relationship can be adopted for cases of Section 3.1. Using Haskind relationship (Falnes and Kurniawan, 2020), the exciting volume flux using the radiation velocity potential

can be determined by

$$Q_e^{(R)} = 2\rho g A^2 \left|R_1^R\right| C_g \,. \tag{46}$$

Considering the case of $G = 0$ (i.e., the perforated wall is considered as an impermeable wall, and there is no dissipative effect), this analytical model must be satisfied by the energy conservation law (i.e., $K_r^2 + \eta = 1$). As is shown in Fig. 3, a good agreement of the exciting volume flux between both methods can be obtained, and the energy flux conservation is satisfied.

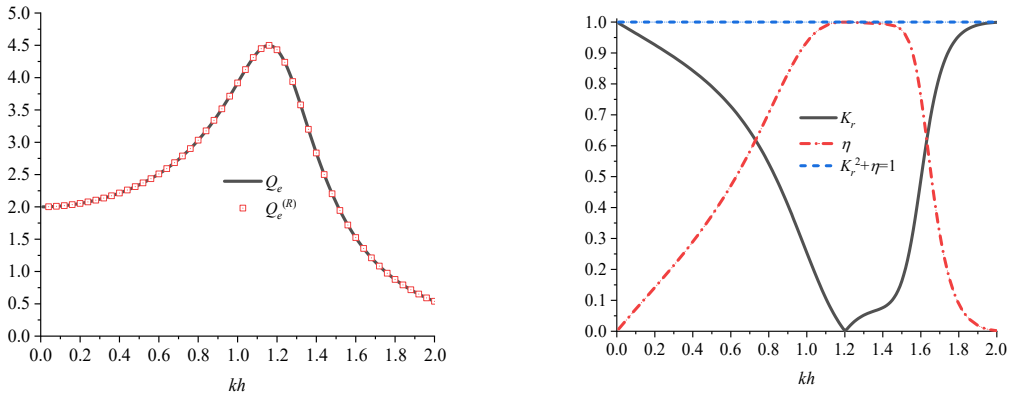

(a) (b)

Fig. 3. (a) the comparison between Q_e and $Q_e^{(R)}$ and (b) result of K_r, η and $K_r^2 + \eta$.

3.3 Comparison between the present model and existing literature

A comparison between the present model and the existing literature was conducted. When $d_1/h = d_2/h \approx 1$, this model is considered as the perforated wall breakwater (Yip and Chwang, 2000). The comparison of K_r is shown in Fig. 4a for $\kappa_1 h = 1.2$ and $G = 1$. When $G \to +\infty$, the perforated thin wall is regarded as a transparent wall, and this model is considered as a harbor/coast-based OWC device (Evans and Porter, 1995a). The comparison of μ is shown in Fig. 4b for $a/h = 1/16$, $d_2/h = 1/2$, $\varepsilon/h = 10^{-3}$ and $G = 10^5$. In addition, the results of this analytical model are also validated by the numerical model (Simonetti and Cappietti, 2021), using the OpenFARM® software package, as shown in Fig. 4c. The geometrical dimensions are set for $d_2/h = 1/2$, $a/h = 1/2$, $\varepsilon/h = 10^{-5}$ and the optimal PTO damping. therefore, a good agreement between the present analytical model and the published results can be achieved.

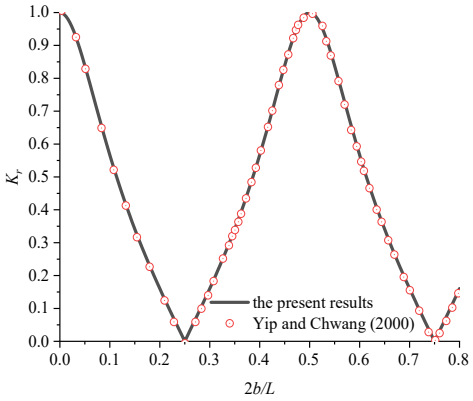

(a) reflection coefficient K_r

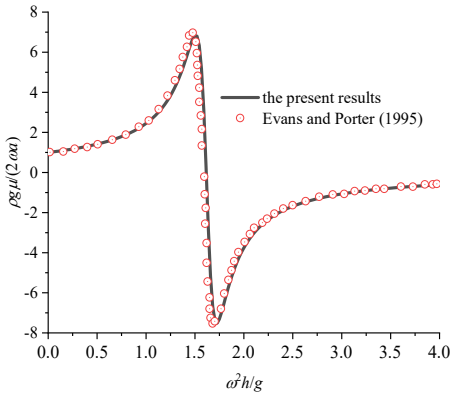

(b) radiation susceptance μ

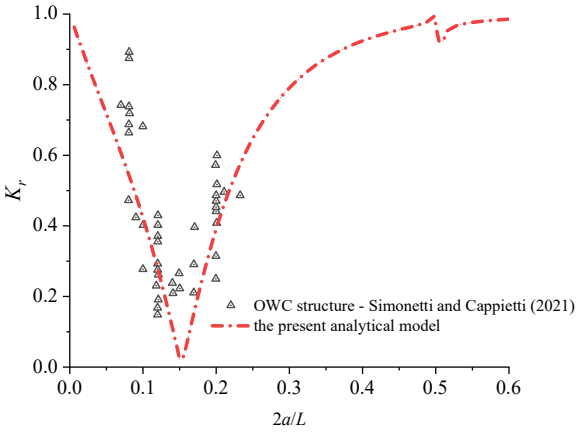

(c) reflection coefficient K_r

Fig. 3. Comparisons between the present results and (a) Yip and Chwang (2000), (b) Evans and Porter (1995a), and (c) Simonetti and Cappietti (2021).

4 Results and discussions

4.1 The effect of porosity coefficient G

The performance of a single OWC device mainly relies on the natural resonance of the OWC, mostly in lower-frequency region (Evans and Porter, 1995a). The porosity coefficients $G = 0$ and ∞ (i.e., 10^5) are regarded as a single OWC device with and without a solid wall. Reflection coefficient K_r, dissipation coefficient K_d, hydrodynamic efficiency η, horizontal wave force F_H, and bending moment M_1 are plotted in Fig. 5 for different porosity coefficients. The geometrical parameters are selected as $d_1/h = d_2/h = 1/2$, $a/h = 1/4$, $\varepsilon/h = 1/20$, $b/h = 1/8$ with the optimal PTO damping.

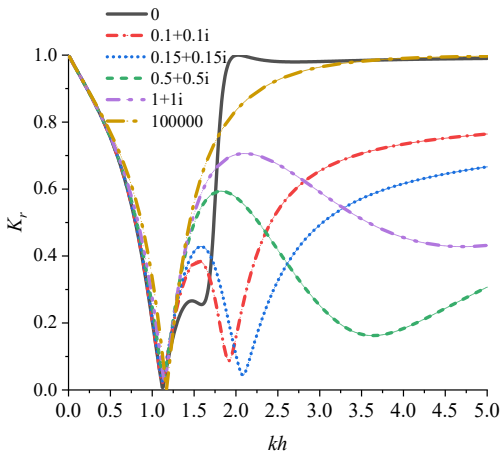

(a) reflection coefficient K_r

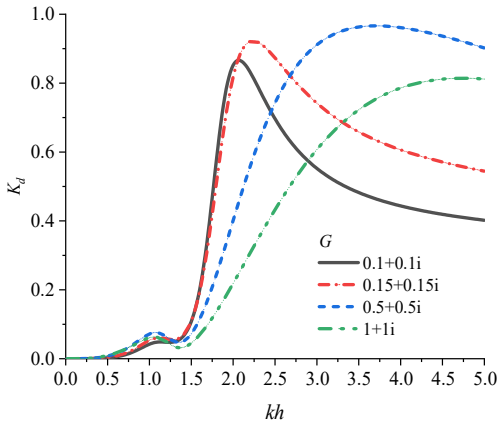

(b) dissipation coefficient K_d

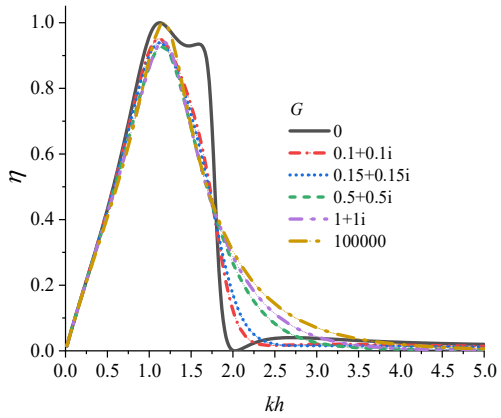

(c) hydrodynamic efficiency η

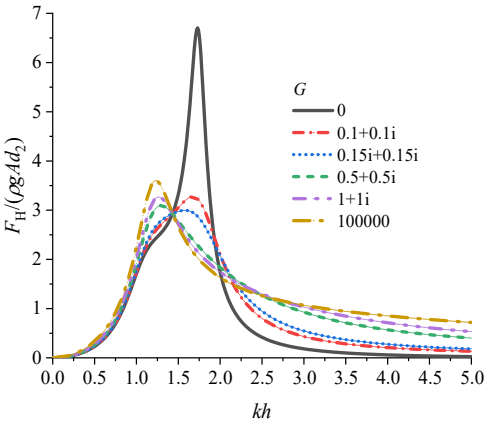

(d) horizontal wave force F_H

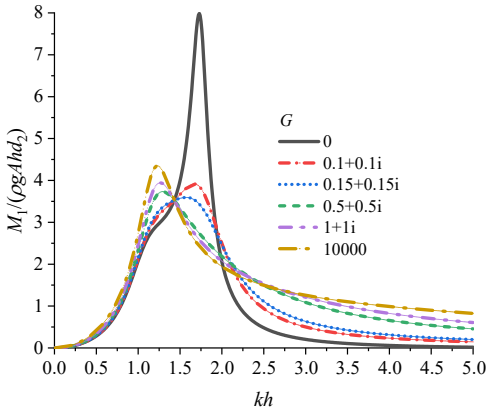

(e) bending moment M_1

Fig. 5. Results of reflection coefficient K_r, dissipation coefficient K_d, hydrodynamic efficiency η, horizontal wave force F_H, and bending moment M_1 for G = 10^5, 1+1i, 0.5+0.5i, 0.15+0.15i, 0.1+0.1i and 0.

For G = 0 and 10^5, the effective frequency bandwidth of the lower reflection is narrower, which is not beneficial to reduce the harbor agitation. A reduction in K_r (i.e., minimum of zero) is due to the function of wave power extraction. Therefore, the wave attenuation performance of an isolated WEC device is related to the natural resonance in the lower frequency region but is considered as a vertical wall structure (K_r = 1.0) in the higher frequency region. In the presence of a perforated wall, K_d increases remarkably. Correspondingly, a reduction (i.e., 83.3%) in K_r (i.e., minimum of 0.167) is found in the higher frequency region, compared with an isolated WEC device. Especially, two valleys of K_r close to zero emerge. For shorter waves, K_r is less than 0.4 for the condition of G = 0.5+0.5i. Therefore, based on the OWC device, the presence of a perforated wall would dissipate the incident wave energy considerably in the higher-frequency region. Interestingly, K_d is not notable at 0.5 < kh < 1.5. This corresponding frequency region dominates a significant role in the bandwidth of the high hydrodynamic efficiency. Therefore, the presence of a perforated wall ineffectively hinders the wave power extraction of an OWC device in the lower frequency region. Comprehensively, an integration between an OWC device and a perforated wall will have a synergy effect between a reduction in wave reflection and satisfactory wave power extraction.

In Fig. 5c, two peaks of η are found for G = 0, and the major benefits are to broaden the bandwidth of the high efficiency significantly. The better wave power extraction implies the less wave reflected from the system. But η is not superior in the higher frequency region. Also, the maximum of F_H and M_1 accompanied by the second peak η is significantly greater than that of a traditional OWC device. This phenomenon is invaluable for the stability of the OWC device. For the presence of a perforated wall, two peaks of η are converted into the only peak value, corresponding to the quasi-piston mode resonance of an OWC device. In the present calculated cases, η, F_H, and M_1 are less than slightly that of an isolated OWC device in the higher frequency region (2.25 < kh < 5.00). A reduction of F_H (i.e., 9.3%) and M_1 (i.e., 17.4%) is found at the piston mode, compared with the OWC device. This phenomenon is due to the wave energy dissipation capacity of a perforated wall, but η modifies moderately. The higher hydrodynamic efficiency may be accompanied by the greater horizontal wave force at the natural resonance of an OWC device. Interestingly, the presence of a perforated wall can mitigate F_H to avoid wave damage,

with the second benefit of moderate change of η.

Variations of wave excitation volume Q_e, radiation susceptance μ, and radiation conductance c are shown in Fig. 6. The first peak η is related to the quasi-piston mode of the water column, accompanied by the peak of Q_e and c nearby (i.e., measuring the energy flux in waves radiating away from the water column oscillating (Falnes and Kurniawan, 2020)). Besides, rapid changes of μ with the occurrence of a negative value are found, associated with near-resonant standing waves inside an OWC chamber. The trigger frequency of the maximum of η is slightly different, which is expected to be close to the natural resonance of single chamber OWC device. This shift phenomenon may be due to wave interaction between the OWC chamber and the dissipative chamber.

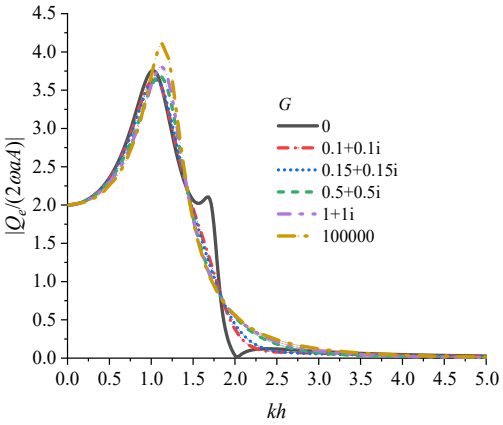

(a) wave excitation volume Q_e

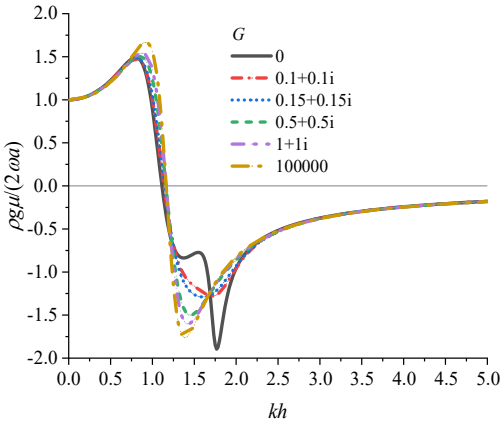

(b) radiation susceptance μ

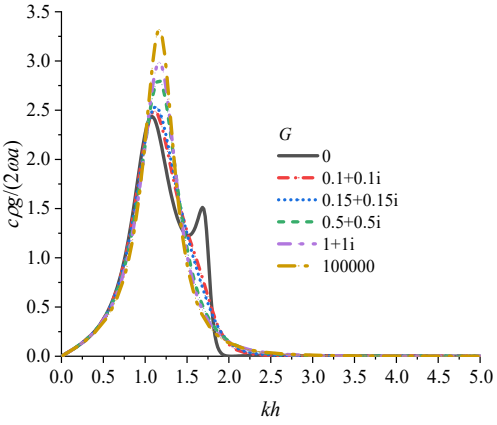

(c) radiation conductance c

Fig. 6. Results of (a) wave excitation volume Q_e, (b) radiation susceptance μ, (c) radiation

conductance c for different porosity coefficients (cases were identical to Fig. 5).

Different from a dual-chamber OWC device, a dissipative chamber composed of the front wall and the perforated wall is not provided with a PTO system. The first peak η depends on the single-chamber OWC device, instead of the equivalent of a single chamber OWC device (consisting of the OWC chamber and the dissipative chamber). For G = 0, the second peak η (at kh = 1.58) is also accompanied by the peak of Q_e and μ nearby, and c appears the variations of 'N' shape. The magnitude of those hydrodynamic coefficients is milder than that of the first peak (in Fig. 6b and 6c). ζ/A at kh = 1.58 for G = 0, 0.1+0.1i and 0.15+0.15i is shown in Fig. 7. The second peak η may be related to the wave resonance trapped inside the dissipative chamber. As G increases, an additional wave resonance is mitigated and peaks of η appear gently. But the wave amplitude inside the OWC chamber is a little different (see Fig. 7). Also, the wave energy transmitted into the dissipative chamber and reflection coefficients decreases, due to the wave energy dissipation capability.

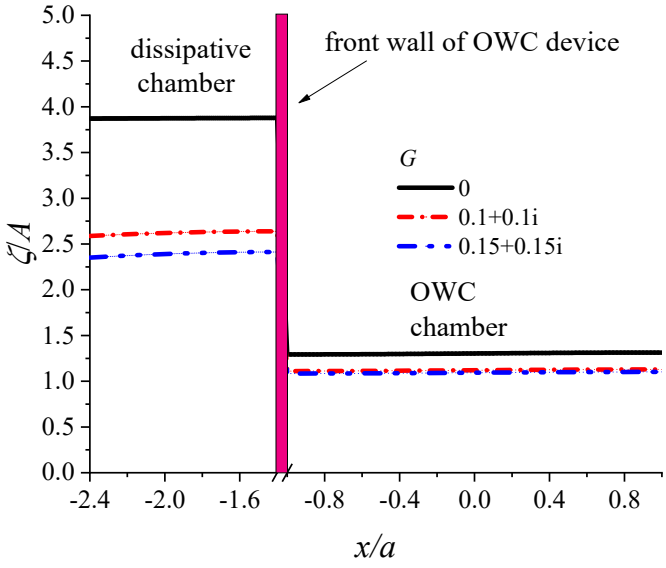

Fig. 7. ζ/A at kh = 1.58 for different porosity coefficients.

4.2 The effect of a dissipative chamber breadth b/h

Results of reflection coefficient K_r, dissipation coefficient K_d, hydrodynamic efficiency η, horizontal wave force F_H, and bending moment M_1 are shown in Fig. 8 for different dissipative chamber breadths b/h = 1/10, 1/2, 1, and 2. The geometrical parameters are selected as d_1/h = d_2/h = 1/2, a/h = 1/4, ε/h = 1/20 and G = 0.15+0.15i. For a traditional perforated structure, the

minimum and maximum of K_r occur at the certain condition of B/L = 0.25+0.5n or 0.5n (Huang et al., 2011), where B and L represent the dissipative chamber length and incident wavelength, respectively. Similarly, the dissipative chamber breadth influences hydrodynamic coefficients among the whole frequency region. A reduction trend of K_r has two valleys for the smaller breadth, but serval peaks and valleys of K_r are found for the greater breadth. K_d has an opposite trend to K_r in the frequency region kh > 2.0. The phenomenon of K_d = 0 (i.e., at kh = 3.15 for b/h = 1/2; kh =1.62, 3.15 and 4.72 for b/h = 1; kh =1.62, 2.37, 3.15, 3.93 and 4.72 for b/h = 2), corresponding to the strong reflection phenomenon, denotes that the perforated wall is considered as 'transparent' wall, which is satisfied by the relation of $2kb = n\pi$ (Huang et al., 2011). Therefore, the dissipative chamber breadth is an integer multiple of half of the wavelength. The function of a perforated wall is invalid. Correspondingly, the conditions of $2kb \approx (n+0.5)\pi$ denote peaks of K_d and valleys of K_r.

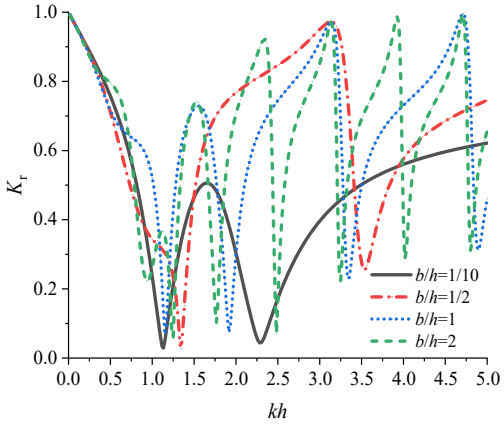

(a) reflection coefficient K_r

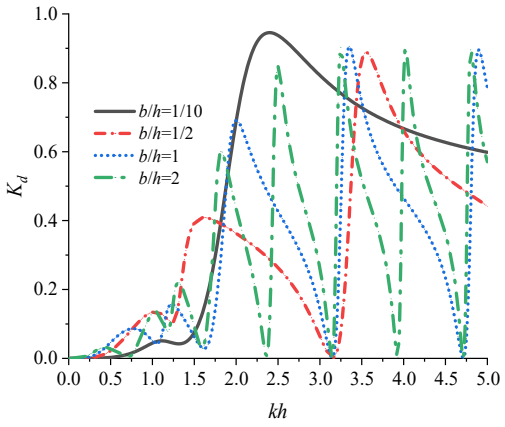

(b) dissipation coefficient K_d

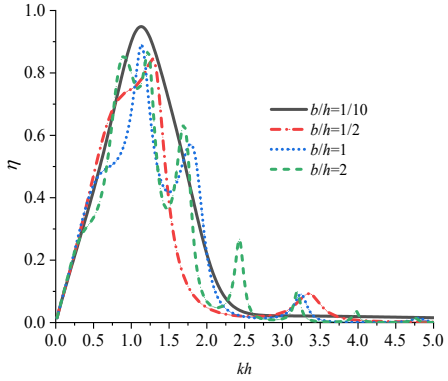

(c) hydrodynamic efficiency η

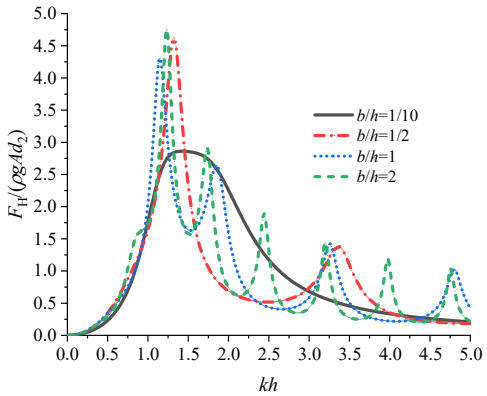

(d) horizontal wave force F_H

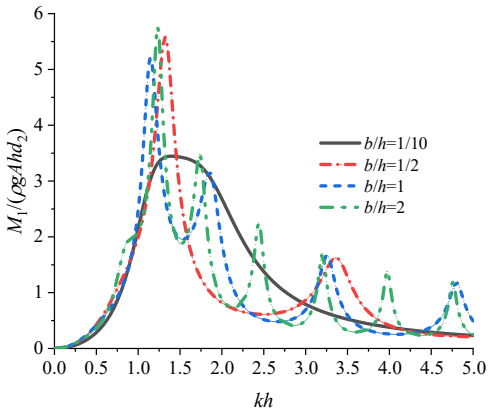

(e) bending moment M_1

Fig. 8. Results of reflection coefficient K_r, dissipation coefficient K_d, hydrodynamic efficiency η, horizontal wave force F_H, and bending moment M_1 for different dissipative chamber breadths.

The only peak of η, F_H and M_1 is found for b/h = 1/10, like Fig. 5. With an increasing b/h, multiple peaks of η emerge in the whole frequency region (b/h = 2 at kh = 0.90, 1.22, 1.70, 2.43, 3.20, 3.97; b/h = 1 at kh = 1.13, 1.78, 3.25, b/h = 1/2 at kh = 1.28, 3.35), but η approaches zero gradually. However, the maximum of F_H and M_1 are greater significance than that of b/h = 1/10 at the piston mode nearby. Detailly, peaks and valleys of K_d are opposite to that of η, F_H, and M_1 nearby. Therefore, the greater dissipative chamber breadth is not beneficial for the benefits of wave reflection reduction. This strong reflection phenomenon should be avoided.

Considering the same geometrical parameters, hydrodynamic coefficients are plotted in Fig. 9 for different incident wavenumber. Those hydrodynamic coefficients appear periodically. The frequency of minima of K_d (i.e., maximum of K_r) is slightly modified, which is satisfied perfectly by $2kb = n\pi$. The corresponding ζ/A is shown in Fig. 10a for $2kb = n\pi$ (n = 2, 3, 4) and kh =2.0. The near-standing wavefield can be formed in the confined area of the dissipative chamber. The number of nodes and antinodes increases with the increasing order of trigger conditions. Also, the amplitude inside the air chamber or additional chamber is identical for different breadths, and the corresponding locations of nodes and antinodes are a little different. The perforated wall may be in wave antinodes. But the trigger of maxima of K_d and minima of K_r is not perfectly satisfied by $2kb = (n + 0.5)\pi$. This is due to the change in phase angle of G. Also, the maximum and minimum of η and F_H are not satisfied perfectly by $2kb = n\pi$ and $(n+0.5)\pi$. With an increasing kh, η and F_H are mitigated. Interestingly, the minima K_r are accompanied by the peak

of η and F_H, at which K_d approaches the peak value. Therefore, a reduction of η and F_H is achieved considering that the most energy is dissipated. For the valley of η and F_H, the corresponding ζ/A is shown in Fig. 10b for $2kb$ = 1.681, 2.648, and 3.667 at kh = 2.0. The overall trend of the peak and valley inside the dissipative chamber is opposite to that in Fig. 10a. The perforated wall may be in wave nodes, and which is not regarded as a fully submerged barrier. Therefore, the perforated wall location is one of the key parameters affecting the hydrodynamic performance of the system, associated with wave dissipation characteristics.

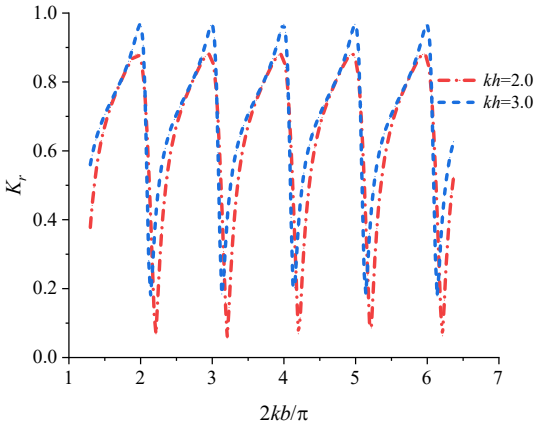

(a) reflection coefficient K_r

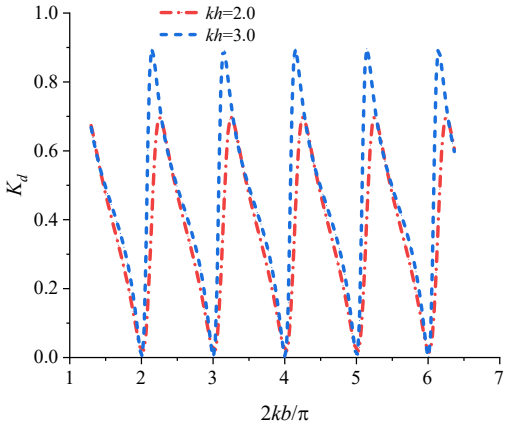

(b) dissipation coefficient K_d

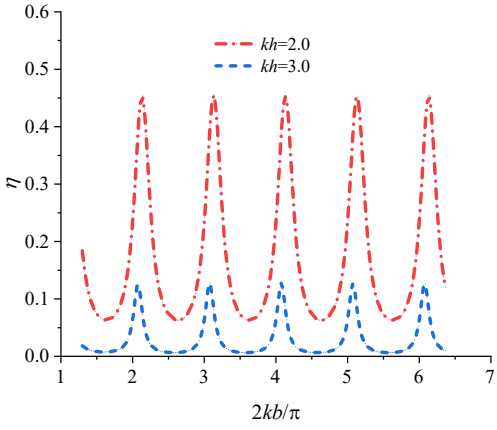

(c) hydrodynamic efficiency η

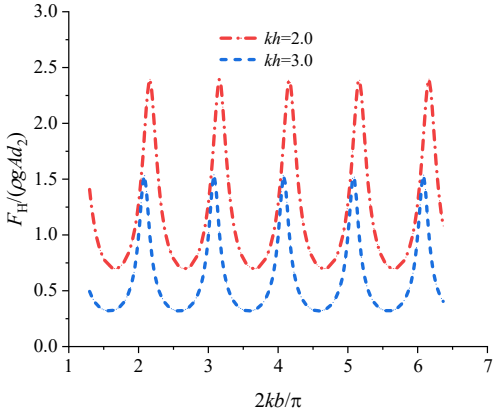

(d) horizontal wave force F_H

Fig. 9. Results of reflection coefficient K_r, dissipation coefficient K_d, hydrodynamic efficiency η, and horizontal wave force F_H for different incident wavenumbers.

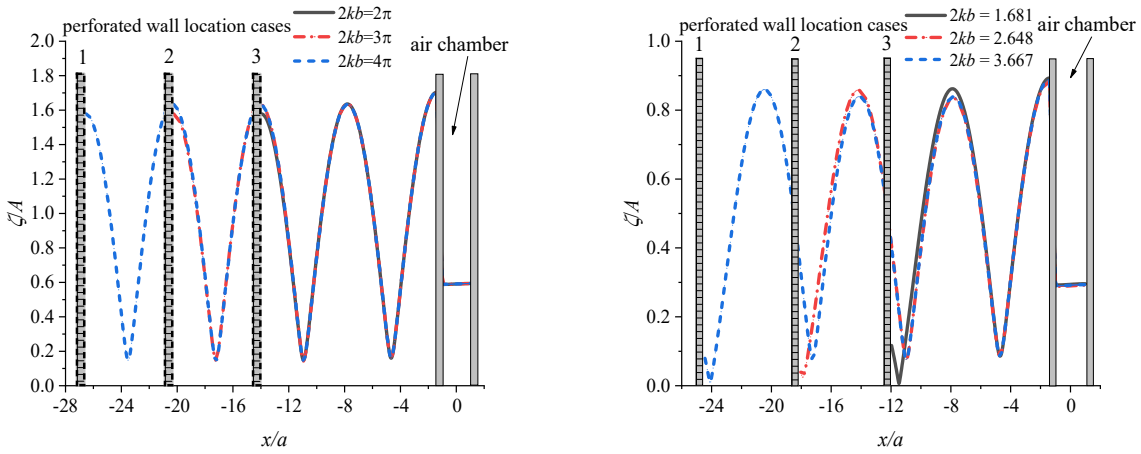

(a) (b)

Fig. 10. The free water surface inside the air chamber and additional chamber.

4.3 The effect of draft of the perforated wall and front wall d_1/d_2

Firstly, this subsection presents the effects of a perforated wall draft on the hydrodynamic performance of this novel OWC structure in Fig. 11. The parameters can be set for d_2/h = 1/2, a/h = 1/4, ε/h = 1/20, b/h = 1/4 and G = 0.15+0.15i. The only valley of K_r emerges for d_1/d_2=9/25, but shape 'W' accompanied by two valleys and one peak is found in the lower frequency region. The first valley K_r corresponding to the first peak of η shifts to the lower frequency region, which is related to quasi-piston resonance. The presence of a perforated wall slightly modifies the natural resonance of an OWC. The second valley of K_r denotes a moderate second peak of η, due to the additional resonance. Also, K_r is a little different for the greater perforated wall draft, less than the case of d_1/d_2 = 9/25. With an increasing d_1/d_2, the maximum of η is mitigated, due to the wave energy dissipation of a perforated wall. However, the maximum of F_H appears downward right after the upward trend slightly. The trend of M_1 is like that of F_H, not plotted. Therefore, variations of a perforated wall draft have little influence on a reduction in F_H and M_1. In the higher frequency region, the perforated wall dominates a significant role in wave reflection reduction. Besides, the capability of energy dissipation is superior with a greater perorated wall draft.

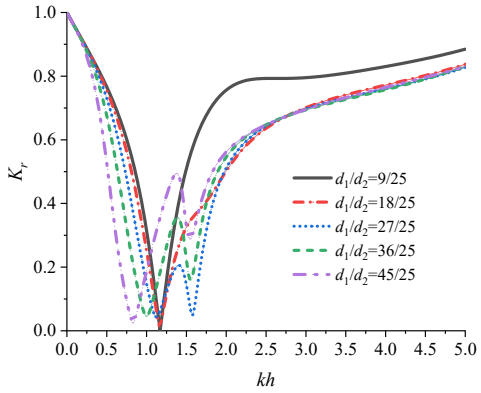

(a) reflection coefficient K_r

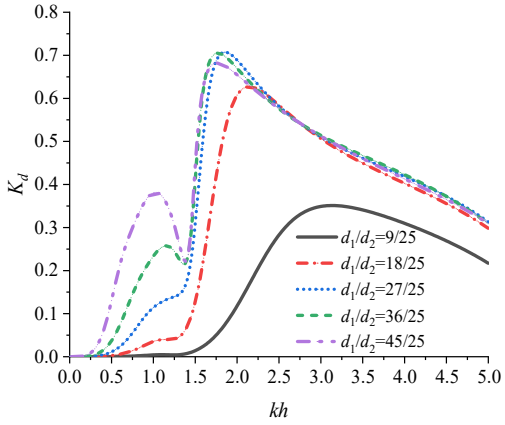

(b) dissipation coefficient K_d

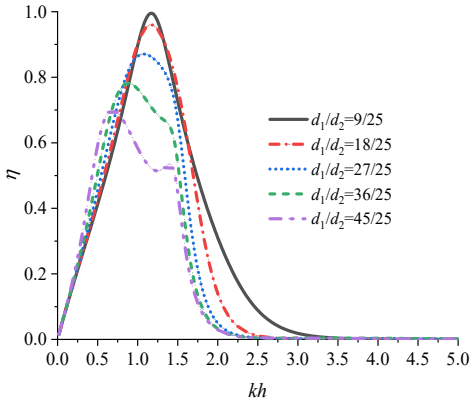

(c) hydrodynamic efficiency η

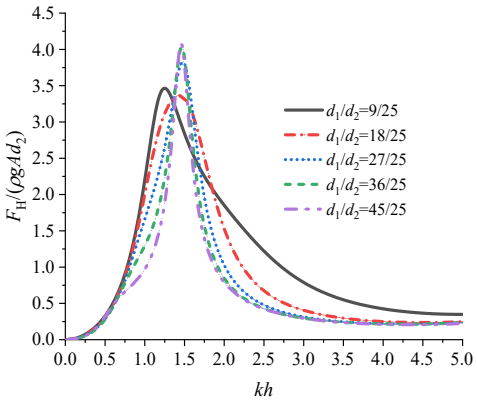

(d) horizontal wave force F_H

Fig. 11. Results of reflection coefficient K_r, dissipation coefficient K_d, hydrodynamic efficiency η, and horizontal wave force F_H for different perforated wall drafts.

The perforated wall draft remains constant. Results of hydrodynamic coefficients are shown in Fig. 12 for different front wall drafts (d_2/d_1 = 9/25, 18/25, 27/25, 36/25 and 45/25). The other dimensions are d_1/h = 1/2, a/h = 1/4, ε/h = 1/20, b/h = 1/4 and G = 1+0.5i. The peak frequency of η and K_r shifts to the lower frequency region. This is due to an increase in the water column volume inside the OWC chamber, resulting in a decrease in the natural frequency. Also, the modification of the front wall draft has a significant effect on wave energy dissipation. The second valley of K_r is accompanied by most incident wave energy dissipation (i.e., a valley of K_d is corresponding to that of K_r). With an increasing front wall draft, the narrower bandwidth of high hydrodynamic efficiency is found, and the maximum of η and F_H increases. Therefore, the smaller front wall draft is beneficial for wave attenuation performance and harbor agitation

reduction, due to the wave power extraction.

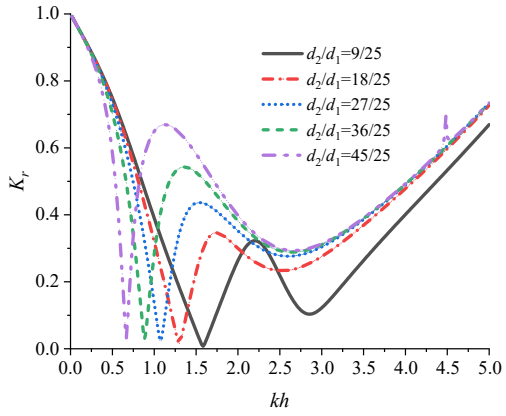

(a) reflection coefficient K_r

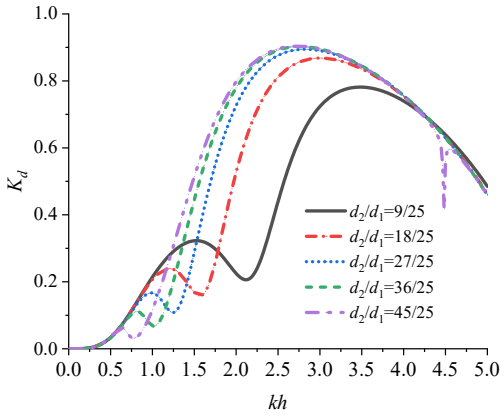

(b) dissipation coefficient K_d

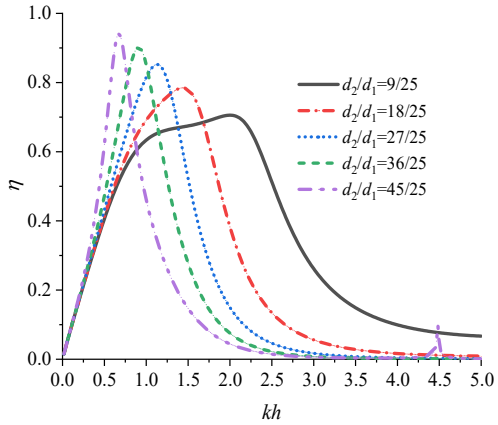

(c) hydrodynamic efficiency η

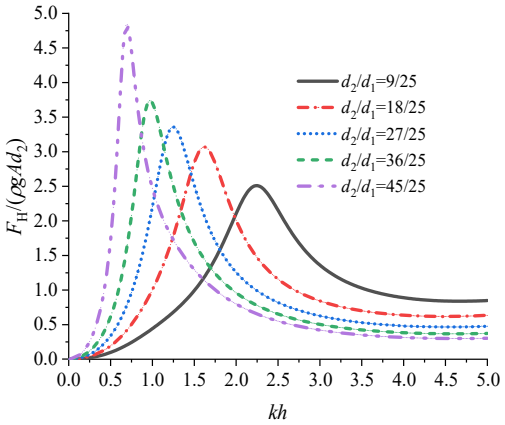

(d) horizontal wave force F_H

Fig. 12. Results of reflection coefficient K_r, dissipation coefficient K_d, hydrodynamic efficiency η, and horizontal wave force F_H for different front wall drafts.

4.4 The effect of air chamber breadth a/h

The air chamber breadth significantly modifies the natural resonance of the OWC device. Results of reflection coefficient K_r, hydrodynamic efficiency η, horizontal wave force F_H, bending moment M_1, radiation susceptance μ, and conductance c are plotted in Fig. 13 for different air chamber breadths a/h = 1/3, 2/3, and 1. The geometrical dimensions are $d_1/h = d_2/h$ = 1/2, ε/h = 1/20, b/h = 1/2, G = 1+1i and optimal PTO damping.

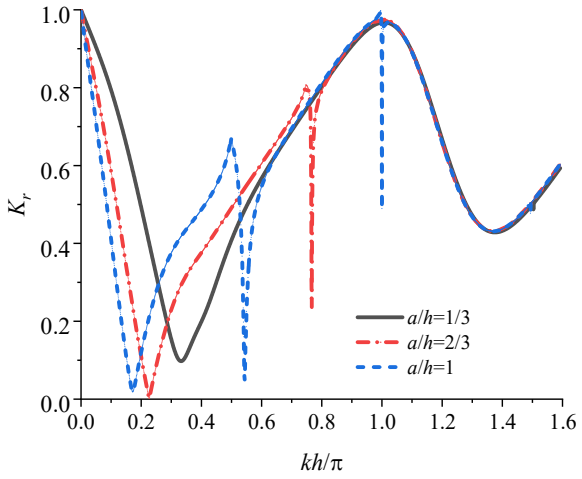

(a) reflection coefficient K_r

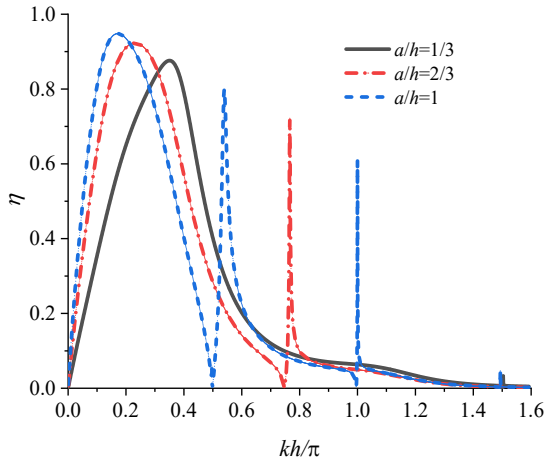

(b) hydrodynamic efficiency η

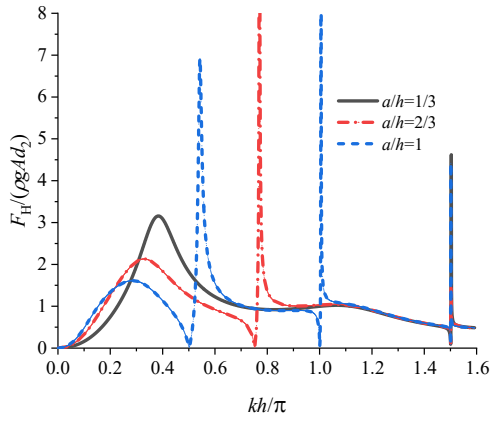

(c) horizontal wave force F_H

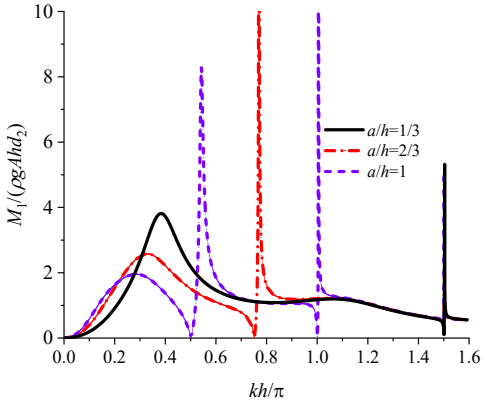

(d) bending moment M_1

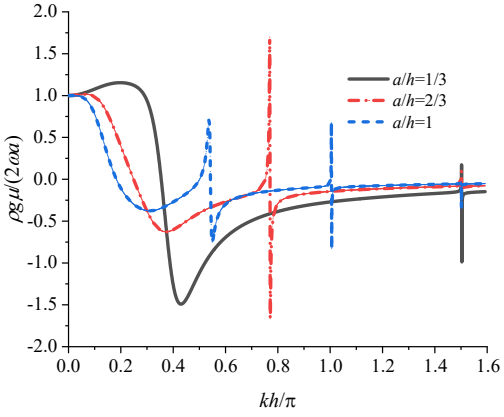

(e) radiation susceptance μ

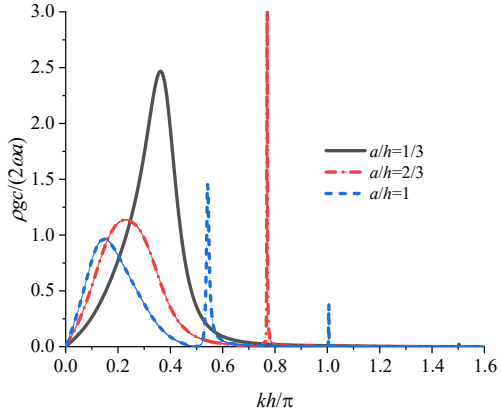

(f) radiation conductance c

Fig. 13. Results of reflection coefficient K_r, hydrodynamic efficiency η, horizontal wave force F_H, bending moment M_1, radiation susceptance μ, and radiation conductance c for different chamber breadths.

The overall trend of K_r is similar for different air chamber breadth, except for some spike values and the shift of the first peak. The trend of η has an opposite to K_r. The first peak of η shifts to the lower frequency region, due to changes of quasi-piston resonance of an OWC chamber. The corresponding η decreases slightly. There exist zeros of η, F_H, and M_1 at $2ka = n\pi$, due to the sloshing mode resonance inside the OWC chamber. Correspondingly, c approaches zeros, representing no waves are radiated to the far-field. Near $\eta = 0$, μ experiences rapid changes from a positive value to a negative value. ζ/A is plotted at $kh = 0.5\pi$ and π for $a/h = 1$ in Fig. 14. The orders of wave nodes are identical to that of the sloshing mode condition. Therefore, the sloshing mode resonance contributes to the strong reflection, cannot be avoided by the presence of a perforated wall.

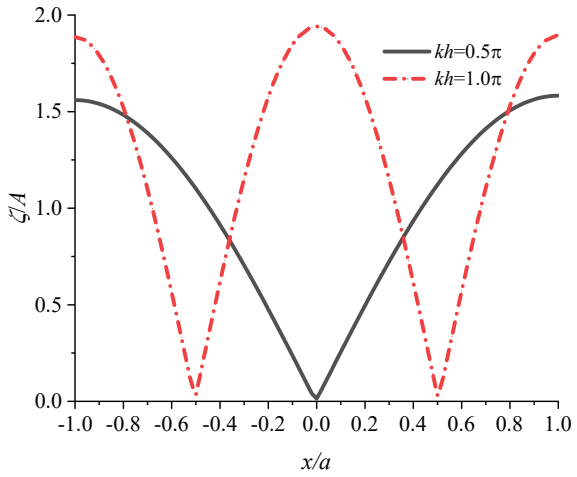

Fig. 14. The ζ/A inside the OWC chamber kh =0.5π and π for a/h = 1.

Some spiked values of K_r and η can be found, where the curve of c passes through zeros twice. The presence of those peaks is attributed to the equation of $\mu + \mu_{pto}$ =0 (i.e., the counteraction of radiation susceptance and air compressibility (Sarmento and De Falcao, 1985; Martins-Rivas and Mei, 2009)), as shown in Fig. 15. Also, F_H and M_1 suddenly experience a jump value, which is harmful to the survival capability of an OWC device. Therefore, the practical engineering design should avoid this sloshing mode resonance phenomenon.

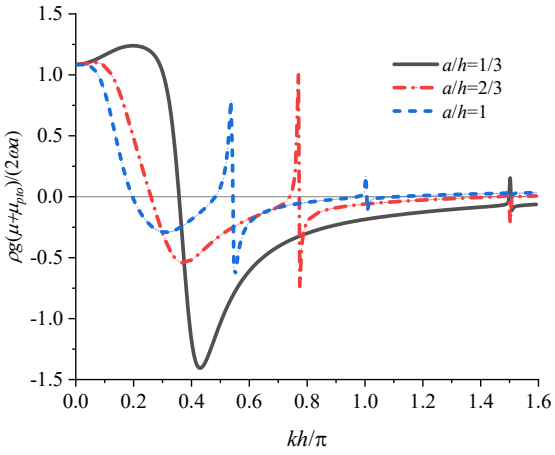

Fig. 15. Results of $\mu + \mu_{pto}$ for different OWC chamber breadths.

4.5 Further discussions

Motivated by methods of dissipating/capturing the incident wave energy (i.e., perforated structure/wave absorber), this paper discussed a novel coastal structure, employed in harbor agitation reduction or coastal protection. This structure can be modified simply by a traditional caisson type breakwater with a defect of greater wave reflection. The windward caisson can be considered as a dissipative chamber with a front perforated wall, and the harbor/coast side caisson is regarded as an air chamber of an OWC device with a PTO system. Compared with an isolated OWC device (Simonetti and Cappietti, 2021), a reduction in wave reflection can be further improved with an additional benefit of the power generation, which may mitigate the wave amplitude inside the harbor and provide a shelter for the ship operation and harbor structure protection. In addition, the presence of a perforated wall may be a promising method to prevent the existing breakwater-OWC device from the wave impact (Medina-López et al., 2015; Falcão and Henriques, 2020; Wang et al., 2020).

For a single OWC as an anti-reflection structure (He and Huang, 2016; Simonetti and Cappietti, 2021), the qualified wave attenuation performance is related to the natural resonance of an OWC device. Owing to the narrower frequency bandwidth of a traditional OWC device, the corresponding frequency region of the lower reflection is limited. Under other cases, the power generation of a device can be neglected, which can be considered as a vertical wall structure. From present theoretical results, a reduction in K_r is accounted for the wave energy capturing of an OWC device mostly in the lower-frequency region (i.e., 100%), as well as the wave energy

dissipation of a perforated wall in the higher-frequency region (i.e., 83.3%), under the proper geometrical configuration.

For a traditional perforated structure, single or multiple dissipative chambers embedded in caissons can be used to dissipate the most incident wave energy (Liu et al., 2016). However, a dissipative chamber of the proposed novel coastal structure may be regarded as a wave accumulation chamber for a smaller G, and an additional resonance inside this chamber is triggered. The broader effective frequency bandwidth of higher hydrodynamic efficiency is found, accompanied by the quasi-piston and additional resonance. The presence of a perforated wall would mitigate the wave gathering behavior slightly.

The wave force acting on the front wall of the OWC chamber is essential to evaluate the stability of an OWC device (John Ashlin et al., 2015; Viviano et al., 2019; Wang et al., 2020). Compared to an isolated OWC device, the maximum of F_{H} diminishes theoretically, especially for the quasi-piston mode and high-frequency region. Therefore, a reduction of F_{H} and M_1 (i.e., 9.3% and 17.4%, respectively) is realized for the qualified stability of the novel structure, with a satisfactory wave power extraction efficiency. The smaller dissipative chamber breadth is more beneficial for a reduction in F_{H}.

To evaluate advantages of this novel structure on the harbor agitation reduction/coastal protection, comparisons of K_r among the present novel structure (Type I), a dissipative chamber with a perforated wall (i.e., bottom-mounted) (Type II), and an isolated OWC WEC device (Type III) are shown in Fig. 16. The conditions are as follow: Type I: $d_1/h = d_2/h = 1/2$, $a/h = 1/3$, $\varepsilon/h = 1/20$, $b/h = 1/5$, $G = 0.3+0.3i$ and $0.4+0.4i$; Type II: $d_2/h = d_1/h \approx 1$, $b/h = 1/2$, $G = 1$ and $1+1i$; Type III: $d_2/h = 1/2$, $a/h = 1/3$, $\varepsilon/h = 1/20$, $G = 10^5$. The dimension of an OWC air chamber remains constant. As indicated in Fig. 16, the effective frequency bandwidth of the lower reflection is narrower for Type III, and $K_r > 0.8$ is found in the frequency region $kh > 2.0$. A coast-land OWC device can be regarded as a vertical wall in the high-frequency region, due to the strong reflection phenomenon. For Type II, valleys and peaks of K_r (i.e., 0 and 1, respectively) appear periodically. Therefore, a perforated wall is limited for the broader incident frequency region, also accompanied by strong reflection. For Type I, a reduction of K_r is not only found in the quasi-piston mode resonance (i.e., 100% due to capturing wave energy), but also in the

higher frequency region (i.e., around 40 - 80% due to dissipating wave energy), compared to Type II or III. The presence of a perforated wall in the front of the OWC device can counteract the shortcoming of the strong reflection phenomenon in the high-frequency region.

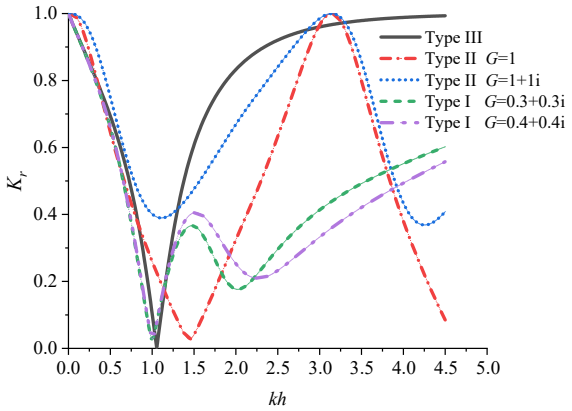

Fig. 16. Comparisons of wave reflection between Type I, II, and III.

From the present theoretical analysis, the novel structure has a synergy effect, comprising of the harbor agitation reduction, mitigation of horizontal wave force acting on the front wall of OWC to further improve the structural stability, and preserving the satisfactory wave power extraction. However, this paper mainly focuses on the hydrodynamic performance for this novel system preliminarily and reveals the influences of the geometrical parameters, based on the linear potential flow theory. In addition, it is worth noting that further study will be carried out on the effect of surface tension, bottom friction or viscosity on the dissipation effect.

A linear PTO damping is applied for wave power extraction in this mathematical model, but the nonlinear PTO damping (Ahamed et al., 2020) is used frequently in practical engineering. The power generation performance should be further estimated by a field test. In addition, the 2D geometrical configuration is considered, in the absence of the along-coast direction length of caissons (i.e., along-coast wave resonance in the 3D model (Liu et al., 2016)). Therefore, the 3D array effect on the hydrodynamic performance of this novel structure will be investigated in the future.

5 Conclusions

The single OWC device embedded in the harbor/coastal structure, provided with a surface-piercing perforated barrier located in the front of the OWC chamber was discussed. Based on the linear potential theory, an analytical model of wave interaction with the novel OWC

structure was developed, using the eigenfunction matching method. The analytical model was validated by Haskind relation, energy conservation, and the existing literature. The influences of geometrical parameters on hydrodynamic coefficients were revealed. The conclusions can be drawn:

1) Wave reflection, horizontal wave force, bending moment are reduced up to 83.3%, 9.3%, and 17.4%, respectively, accompanied by a satisfactory power extraction efficiency, with a proper porosity coefficient, compared with a traditional OWC device. The capability of capturing and dissipating wave energy results in a reduction of the wave reflection for this novel OWC structure, which is beneficial for harbor agitation mitigation, coastal protection, and the structural stability of the device. The presence of the perforated wall slightly decreases the wave power extraction by OWC.
2) It is demonstrated that the quasi-piston resonance inside the OWC air chamber and additional resonance inside the dissipative chamber contribute to a reduction of wave reflection (around 100%) and an increment of wave power extraction efficiency, but with the greater horizontal wave force.
3) The dissipative chamber breadth influences the hydrodynamic characteristics of this novel OWC structure significantly. The near-standing wave field is formed in the confined area. As a perforated wall is located in antinodes (i.e., $2kb = n\pi$), peaks of reflection coefficient denote that a perforated wall is considered as a 'transparent' wall. The valleys of reflection coefficient, corresponding to the peak of wave power extraction efficiency and horizontal wave force are not perfectly satisfied for nodes (i.e., $2kb \approx (n+0.5)\pi$).
4) The novel OWC structure is sensitive to the front wall design instead of the perforated wall, related to the quasi-piston resonance inside the OWC air chamber. The medium draft ratio to a perforated and front wall should be selected to achieve better wave energy dissipation capability and wave power extraction.
5) The multiple orders of sloshing mode resonance inside the OWC chamber are found with an increasing air chamber breadth, accompanied by zeros of power extraction efficiency and spiked value of wave reflection and bending moment. This phenomenon should be avoided in practical engineering. At this certain frequency, however, the presence of a

perforated wall is an ineffective tool to improve the wave attenuation performance of this novel coastal structure.

Based on the theoretical analysis, this paper can provide a preliminary design of this novel coastal structure to reduce the wave reflection in harbor engineering practice and improve the coastal protection, with the second benefit of the wave power extraction and better structural stability.

Acknowledgements

The work is supported by the National Natural Science Foundation of China (52001086), the Key Program for International Scientific and Technological Innovation Cooperation between Governments (2019YFE0102500), and the China Postdoctoral Science Foundation Funded Project (2019M661257).

References

Ahamed, R., McKee, K., Howard, I., 2020. Advancements of wave energy converters based on power take off (PTO) systems: a review. Ocean Engineering. 204, 107248.

Altomare, C., Gironella, X., 2014. An experimental study on scale effects in wave reflection of low-reflective quay walls with internal rubble mound for regular and random waves. Coastal Engineering. 90, 51-63.

Boccotti, P., 2012. Design of breakwater for conversion of wave energy into electrical energy. Ocean Engineering. 51, 106-118.

Evans, D.V., Porter, R., 1995a. Hydrodynamic characteristics of an oscillating water column device. Applied Ocean Research. 17(3), 155-164.

Evans, D.V., Porter, R., 1995b. Complementary approximations to wave scattering by vertical barriers. Journal of Fluid Mechanics. 294, 155-180.

Falcão, A.F.O., Sarmento, A.J.N.A., Gato, L.M.C., Brito-Melo, A., 2020. The Pico OWC wave power plant: its lifetime from conception to closure 1986-2018. Applied Ocean Research. 98, 102104.

Falnes, J. and Kurniawan A. 2020. Ocean waves and oscillating systems: linear interactions including wave-energy extraction. Cambridge University Press.

He, F., Huang, Z., 2016. Using an oscillating water column structure to reduce wave reflection from a vertical wall. Journal of Waterway, Port, Coastal and Ocean Engineering. 142(2): 04015021.

Huang, Z., Li, Y., Liu, Y., 2011. Hydraulic performance and wave loadings of perforated/slotted coastal structures: a review. Ocean Engineering. 38(10), 1031-1053.

John Ashlin, S., Sannasiraj, S.A., Sundar, V., Sundar, V., Sannasiraj, S.A., Murali, K., Sriram, V., 2015. wave forces on an oscillating water column device. Procedia Engineering. 116, 1019–1026.

Lee, J.I., Shin, S., 2014. Experimental study on the wave reflection of partially perforated wall caissons with single and double chambers. Ocean Engineering. 91, 1-10.

Liu, Y., Li, Y.C., Teng, B., 2016. Interaction between oblique waves and perforated caisson breakwaters with perforated partition walls. European Journal of Mechanics, B/Fluids. 56, 143-155.

Liu, Y., Yoshida, S., Hu, C., Sueyoshi, M., Sun, L., Gao, J., Cong, P., He, G., 2018. A reliable open-source package for performance evaluation of floating renewable energy systems in coastal and offshore regions. Energy Conversion and Management. 174, 516-536.

Liu, Y., Li, Y.C., 2011. Wave interaction with a wave absorbing double curtain-wall breakwater. Ocean Engineering. 38(10), 1237-1245.

López, I., Rosa-Santos, P., Moreira, C., Taveira-Pinto, F., 2018. RANS-VOF modelling of the hydraulic performance of the LOWREB caisson. Coastal Engineering. 140, 161-174.

Lyu, Z., Liu, Y., Li, H., Mori, N., 2020. Iterative multipole solution for wave interaction with submerged partially perforated semi-circular breakwater. Applied Ocean Research. 97, 102103.

Martins-Rivas, H., Mei, C.C., 2009. Wave power extraction from an oscillating water column at the tip of a breakwater. Journal of Fluid Mechanics. 626, 395-414.

Medina-López, E., Allsop, W., DImakopoulos, A., Bruce, T., Wallendorf, L., Cox, D.T., 2015. Conjectures on the failure of the OWC breakwater at Mutriku. Coastal Structures and Solutions to Coastal Disasters Joint Conference. Boston, USA, 9-11 September, 592-603.

Melikoglu, M., 2018. Current status and future of ocean energy sources: a global review. Ocean Engineering. 148, 563-573.

Mustapa, M.A., Yaakob, O.B., Ahmed, Y.M., Rheem, C., Koh, K.K., Adnan, F.A., 2017. Wave energy device and breakwater integration: a review. Renewable and Sustainable Energy Reviews. 77, 43-58.

Neelamani, S., Al-Salem, K., Taqi, A., 2017. Experimental investigation on wave reflection characteristics of slotted vertical barriers with an impermeable back wall in random wave fields. Journal of Waterway, Port, Coastal and Ocean Engineering. 143(4): 06017002.

Ning, D., Zhou, Y., Zhang, C., 2018. Hydrodynamic modeling of a novel dual-chamber OWC wave energy converter. Applied Ocean Research. 78, 180-191.

Ning, D.Z., Zhou, Y., Mayon, R., Johanning, L., 2020. Experimental investigation on the hydrodynamic performance of a cylindrical dual-chamber oscillating water column device. Applied Energy. 260: 114252.

Ning, D.Z., Zhao, X.L., Teng, B., Johanning, L., 2017. Wave diffraction from a truncated cylinder with an upper porous sidewall and an inner column. Ocean Engineering. 130, 471-481.

Pawitan, K.A., Dimakopoulos, A.S., Vicinanza, D., Allsop, W., Bruce, T., 2019. A loading model for an OWC caisson based upon large-scale measurements. Coastal Engineering. 145, 1-20.

Rezanejad, K., Bhattacharjee, J., Guedes Soares, C., 2015. Analytical and numerical study of dual-chamber oscillating water columns on stepped bottom. Renewable Energy. 75, 272-282.

Sarmento, A.J.N.A., De Falcao, A.F.O., 1985. Wave generation by an oscillating surface-pressure and its application in wave-energy extraction. Journal of Fluid Mechanics. 150, 467-485.

Simonetti, I., Cappietti, L., 2021. Hydraulic performance of oscillating water column structures as anti-reflection devices to reduce harbour agitation. Coastal Engineering. 165: 103837.

Sollitt, C.K., Cross, R.H., 1972. Wave transmission through permeable breakwaters. In: Proceedings of the 13th International Conference Coastal Engineering, ASCE, New York,

pp.1 847–1865.
Teixeira, P.R.F., Didier, E., 2021. Numerical analysis of the response of an onshore oscillating water column wave energy converter to random waves. Energy. 220, 119719.
Theocharis, I., Anastasaki, E.N., Moutzouris, C.I., Giantsi, T., 2011. A new wave absorbing quay-wall for wave height reduction in a harbor basin. Ocean Engineering. 38(17-18), 1967-1978.
Tsai, C.P., Ko, C.H., Chen, Y.C., 2018. Investigation on performance of a modified breakwater-integrated OWC wave energy converter. Sustainability (Switzerland). 10(3), 643.
Viviano, A., Musumeci, R.E., Vicinanza, D., Foti, E., 2019. Pressures induced by regular waves on a large scale OWC. Coastal Engineering. 152, 103528.
Wang, R.Q., Ning, D.Z., Zou, Q.P., 2020. Wave loads on a land-based dual-chamber oscillating water column wave energy device. Coastal Engineering. 160, 103744.
Yip, T.L., Chwang, A.T., 2000. Perforated wall breakwater with internal horizontal plate. Journal of Engineering Mechanics. 126(5), 533-538.
Yu, X.P., 1995. Diffraction of water waves by porous breakwaters. Journal of Waterway, Port, Coastal, and Ocean Engineering. 121 (6), 275–282.
Zhao, X., Zhang, Y., Li, M., Johanning, L., 2021a. Experimental and analytical investigation on hydrodynamic performance of the comb-type breakwater-wave energy converter system with a flange. Renewable Energy. 172, 392–407.
Zhao, X., Xue, R., Geng, J., Göteman, M., 2021b. Analytical investigation on the hydrodynamic performance of a multi-pontoon breakwater-WEC system. Ocean Engineering. 220, 108394.
Zhao, X.L., Ning, D.Z., Zou, Q.P., Qiao, D.S., Cai, S.Q., 2019. Hybrid floating breakwater-WEC system: a review. Ocean Engineering. 186, 106126.